metals

MDPI

Article

Heat Treatment Effect on the Corrosion Resistance of 316L Stainless Steel Produced by Laser Powder Bed Fusion

Kevin Sangoi [1], Mahdi Nadimi [1], Jie Song [2,*] and Yao Fu [1,3,*]

[1] Department of Aerospace and Ocean Engineering, Virginia Polytechnic Institute and State University, Blacksburg, VA 24061, USA; skevin98@vt.edu (K.S.); mnadimi@vt.edu (M.N.)
[2] College of Engineering, SUNY Polytechnic Institute, Utica, NY 13502, USA
[3] Department of Materials Science and Engineering, Virginia Polytechnic Institute and State University, Blacksburg, VA 24061, USA
* Correspondence: jie.song@sunypoly.edu (J.S.); yaof@vt.edu (Y.F.)

Abstract: This study explores the effect of heat treatment on the microstructural characteristics and corrosion resistance of 316L stainless steels (SSs) produced via laser powder bed fusion (L-PBF), focusing on anisotropic corrosion behavior—a relatively less explored phenomenon in LPBF 316L SSs. By systematically analyzing the effects of varying heat treatment temperatures (500 °C, 750 °C, and 1000 °C), this work uncovers critical correlations between microstructural evolution and corrosion properties. The findings include the identification of anisotropic corrosion resistance between horizontal (XY) and vertical (XZ) planes, with the vertical plane demonstrating higher pitting and repassivation potentials but greater post-repassivation current densities. Furthermore, this study highlights reductions in grain size, dislocation density, and melt pool boundaries with increasing heat treatment temperatures, which collectively diminishes corrosion resistance. These insights advance the understanding of processing–structure–property relationships in additively manufactured metals, providing practical guidelines for optimizing thermal post-processing to enhance material performance in corrosive environments.

Keywords: heat treatment; corrosion resistance; additive manufacturing; laser powder bed fusion; 316L stainless steel; pitting corrosion; corrosion fatigue; material characterization

Academic Editor: Branimir N. Grgur

Received: 20 November 2024
Revised: 26 December 2024
Accepted: 2 January 2025
Published: 4 January 2025

Citation: Sangoi, K.; Nadimi, M.; Song, J.; Fu, Y. Heat Treatment Effect on the Corrosion Resistance of 316L Stainless Steel Produced by Laser Powder Bed Fusion. *Metals* **2025**, *15*, 41. https://doi.org/10.3390/met15010041

1. Introduction

The advent of advanced manufacturing techniques, such as 3D printing, particularly laser powder bed fusion (L-PBF), has significantly altered the manufacturing landscape by enabling the production of complex geometries and the optimization of material properties that were previously challenging or impossible to achieve. Among the materials benefiting from these advancements is 316L stainless steel, known for its exceptional corrosion resistance. This material finds critical applications in environments where corrosion is a significant concern, such as in biomedical implants, nuclear reactor components, and marine hardware. Its prominence in these areas is attributed to its reliability and versatility, making it worth extensive research, especially in the growing field of 3D printing [1–5].

The rapid heating and cooling cycles inherent to the L-PBF process induce unique microstructural features, such as cellular dislocation networks, solute segregation at sub-grain boundaries, and a heterogeneous distribution of oxides and inclusions. These attributes impart superior mechanical strength but also affect corrosion resistance, often in ways distinct from conventionally processed stainless steels [6–10]. Previous research in this domain has laid a solid foundation by comparing the corrosion and mechanical properties of

conventionally manufactured 316L with those produced through additive manufacturing, mainly focusing on variations in printing parameters [6–9]. These studies have highlighted the influence of pore characteristics on crack propagation and delved into the role of various microstructural parameters, such as crystallographic texture, grain orientation, dislocation networks, solute segregation, and residual stresses, in determining the corrosion resistance of the material [6,10–15]. Gnanasekaran [6] explored the corrosion and fatigue resistance of 316L stainless steel processed by L-PBF, indicating that porosity may increase metastable pitting but does not diminish pitting resistance due to the microstructural benefits such as strong texture and dislocation networks. Song [15] further elaborates on the benefits of L-PBF, showing that layering one to six layers enhances pitting resistance by forming a robust passive film and dense dislocation patterns, in contrast to traditional manufacturing methods. Conversely, Laleh [16] found that the pitting corrosion resistance of L-PBF 316L stainless steel decreased significantly after thermal post-processing at temperatures above 1000 °C. This setback was attributable to the formation of MnS inclusions, thus highlighting the balance between manufacturing techniques and thermal treatment in preserving material integrity.

The intricate relationship between heat treatment and the microstructural and corrosion properties of 316L stainless steel fabricated via laser powder bed fusion (L-PBF) remains a key area of research. Recent work [11,12,17–20] revealed that micro-segregation of Mo leads to a deficiency of elements in adjacent regions, promoting the growth of pits in the depth region. As heat treatment increases, Mo and other elements are distributed more evenly and become homogenized. This helps in the formation of Mo oxides, which repair and slow down the acceleration of pitting in the material. Micro-segregation is also known to affect the passive film layer. As the micro-segregation of Mo increases, the concentration of defects also increases. Additionally, Kong et al. [21] highlighted the critical role of molybdenum in stabilizing passive films, mitigating localized corrosion, and enhancing polarization resistance in additively manufactured 316L stainless steel. Wang et al. [22] demonstrated that subcritical annealing (800 °C) improved pitting resistance by homogenizing the microstructure, whereas higher temperatures (e.g., 1100 °C) reduced resistance due to the coarsening of inclusions and formation of chromium-depleted zones. Similarly, Bedmar et al. [23] highlighted the detrimental effects of grain growth and oxide inclusion formation at elevated temperatures on polarization resistance, emphasizing the need for optimized post-processing strategies. Ronneberg et al. [24] revealed that heat treatment within specific temperature regimes dissolves melt pool boundaries and reduces dislocation densities, enhancing mechanical performance. Dong et al. [25] explored the influence of heat treatment on stress corrosion cracking (SCC) susceptibility, emphasizing the role of residual stress relief and build orientation in anisotropic corrosion behavior. Their findings align with Kluczyński et al. [26], who demonstrated that hot isostatic pressing effectively reduces porosity, indirectly improving corrosion resistance. Sun et al. [27] and Li et al. [28] further emphasized the importance of controlling thermal post-processing to balance strength, ductility, and corrosion resistance. While Sun [27] examined the influence of thermal treatments on elemental redistribution and oxide stability in related alloys, Li et al. [28] observed significant microstructural stability improvements within the 650 °C to 900 °C temperature range.

Despite these advancements, studies on the effect of heat treatment on microstructure and corrosion performance still lack consideration of anisotropic corrosion performance at different build planes as a function of heat treatment temperature. This study systematically examines the microstructural features and pitting performance of heat-treated L-PBF 316L stainless steel after being heat treated at 500 °C, 750 °C, and 1000 °C, respectively. Electron backscatter diffraction (EBSD) analysis and transmission electron microscopy

(TEM) were employed to thoroughly examine the microstructure in both horizontal and vertical planes. Electrochemical polarization tests provide insights into the correlation of heat treatment with corrosion performance, characterized by the pitting and repassivation potential. Consequently, this study aims to develop a more in-depth understanding of how high-temperature environments impact the microstructural integrity of 316L and its overall performance and durability, bridging critical knowledge gaps and offering practical insights for optimizing thermal post-processing strategies.

2. Materials and Methods

2.1. Sample Preparation

Utilizing AISI 316L stainless steel powders provided by Linde AMT (Indianapolis, IN, USA), specimens measuring 50 × 50 × 60 mm were produced using an EOS M290 (Krailling, Germany). This equipment maintains a constant laser beam of 100 microns and operates within a 70% argon-filled inert environment. The construction orientation was set along the Z-axis (vertically), with the scanning layers being applied on the XY plane (horizontally). The process involves a 67° rotation scanning approach between each layer. Layers were uniformly set at a thickness of 20 microns. The parameters used in the process included a power setting (P) of 150W, hatch spacing (H) of 50 microns, and a scanning speed (V) of 1083 mm/s. The samples were then heat treated at 250, 500, 750, and 1000 °C for 16 h, respectively.

2.2. Electrochemical Corrosion Testing

For the electrochemical corrosion evaluation, the test samples were coated in epoxy resin, leaving an exposed area of 0.32 cm^2, and then polished to a P2400 grit level. The testing setup included a three-electrode system using a graphite counter electrode and a saturated calomel reference electrode (SCE). All potential measurements in this study are referenced against the SCE. The experimental solution was a 3.5 wt.% NaCl (0.61 M), with a pH of around 5.8. These tests were conducted at ambient temperature with natural aeration. Polarization tests were performed at a scanning rate of 0.1667 mV/s, starting from −150 mV relative to the open circuit potential (OCP). Cyclic polarization tests followed the same initial rate and starting point, reversing the scan when the current density hit 0.5 mA/cm2 at a reverse rate of 1.667 mV/s. All electrochemical data were captured using a Gamry potentiostat/galvanostat. To ensure reproducibility and minimize errors, the sample surface and solution were prepared using the same standard prior to each test. The sample surfaces were polished to a P2400 grit level, cleaned with deionized water, and then dried before immersion in the solution. To prevent crevice corrosion and ensure that pitting occurred within the interior of the sample surface during the cyclic polarization test, the center of the surface was first protected with circular adhesive paper. A passive film was then formed on the annular area by polarization within the passive regime. Afterward, the sample was removed from the solution, the adhesive paper was removed, and the circular center area was cleaned with ethanol. Finally, the sample was returned to the solution for the cyclic polarization test. This approach ensured that pitting occurred primarily within the circular center area rather than at the interface between the epoxy and metal. Each measurement was repeated at least three times. Up to six experiments were conducted for certain conditions where the first three tests showed inconsistent results. The presented results represent the average of a minimum of three trials.

2.3. Testing for Evaluation of Microstructural Features

The microstructural analysis of the specimens involved scanning electron microscopy (SEM) and EBSD. To prepare the samples for SEM/EBSD examination, they underwent

electropolishing using a mixture containing 12.5% sulfuric acid and 87.5% methanol. This process was performed at a voltage of 50 V and ambient temperature. Following electropolishing, the samples were electrolytically etched in a solution of 10% saturated oxalic acid, applying 12 V for a duration of 90 s. For samples intended for TEM analysis, the preparation involved using a twin-jet polisher with a solution composed of 10 parts perchloric acid, 45 parts methanol, and 45 parts glacial acetic acid by volume at 228 K and a potential of 15 V. TEM observation was realized through JEOL JEM 2100 (Peabody, MA, USA) at 200 kV.

3. Results and Discussion

3.1. Results

3.1.1. Microstructural Characterization

Figure 1 shows the SEM images of all samples at different heat treatment temperatures. The melt pool boundaries are clearly visible in the as-fabricated (AF) condition and remain so until heat treated at 500 °C (Figure 1). However, the melt pool boundaries begin to fade at 750 °C and cannot be identified at 1000 °C. The microstructure of the samples in their AF state, as well as after heat treatment at 500 °C and 750 °C, displays fan-shaped melt pools characteristic of L-PBF samples (Figure 1). These distinct fan-shaped pools result from the successive track-by-track and layer-by-layer building methods inherent to the L-PBF technique [29]. No microstructural changes were observed between the sample aged at 250 °C and the AF condition. Hence, the experimental results for the 250 °C study have been excluded for further analysis. Figure 2 represents a comparison of grain size for the AF and AF + aged samples. The grain sizes in the XY plane were 25.32 ± 14.14 µm, 23.86 ± 14.45 µm, 23.52 ± 13.13 µm, and 20.36 ± 10.19 µm for the AF, AF + aged 500 °C, AF + aged 750 °C, and AF + aged 1000 °C, respectively. In comparison, the grain sizes in the XZ plane were 92.01 ± 67.98 µm, 75.93 ± 48.49 µm, 43.6 ± 27.1 µm, and 45.14 ± 29.94 µm for the AF, AF+ 500 °C aged, AF + 750 °C aged, and AF + 1000 °C aged conditions, respectively. It is worth noting that these results contrast with [30], where an increase in grain size was reported.

EBSD-IPF and grain images, as illustrated in Figure 3 for the XZ plane, with a resolution scale of 400 microns, enabled the analysis of grain orientation in 316L stainless steel samples through a color-coded scheme based on crystal lattice orientation. The XY cross-section of the columnar grain exhibits an equiaxed feature, which remains unchanged after heat treatment. In the as-built condition, the grain structure appears coarsest. A gradual transition occurs with increasing heat treatment temperature. The grain structure images, as shown in Figure 4 for the XZ plane, demonstrate columnar grains. This grain size variation is consistent with that observed on the XY plane, where an increase in temperature correlates with a transformation from coarse to finer grains.

The contour pole figure (PF) collected on the XZ planes (parallel to the build direction) measures the texture strength for the three families of planes of FCC on {001}, {110}, and {111}, as shown in Figure 5. In the AF condition, an as-built texture with a {101} plane orientation parallel to the build direction was developed. However, the texture began to diminish at AF + aged 750 °C and AF + aged 1000 °C. The maximum multiple of uniform density (MUD) is 6.935 in the AF condition. As the heat treatment temperature increases, the MUD gradually decreases to 6.646, 3.805, and 3.177, respectively, when aged at 500 °C, 750 °C, and 1000 °C. It is worth noting that a fully equiaxed grain structure has a MUD of around 1. Thus, the as-built {101} texture gradually diminishes with increasing heat treatment temperature.

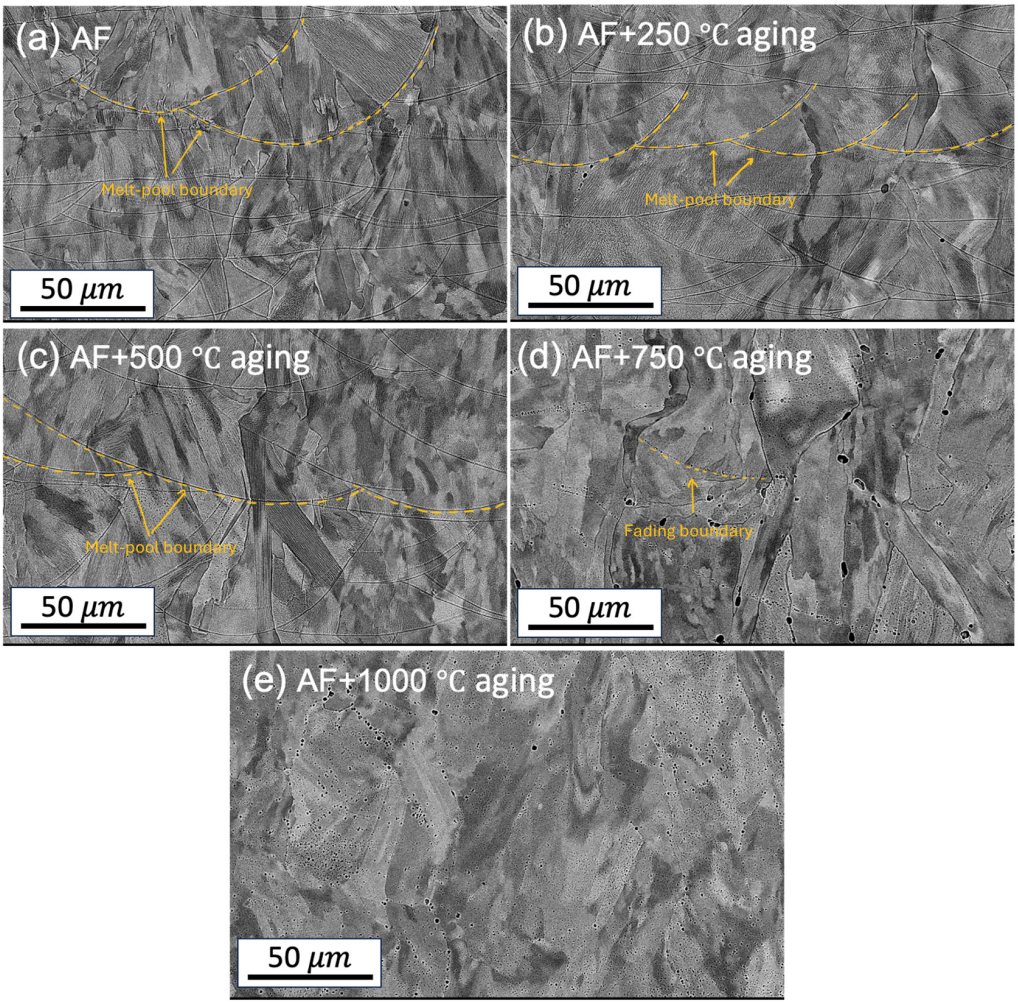

Figure 1. SEM images of the (**a**) AF and (**b**–**e**) AF + aged samples (XZ plane) at different heat treatment temperatures.

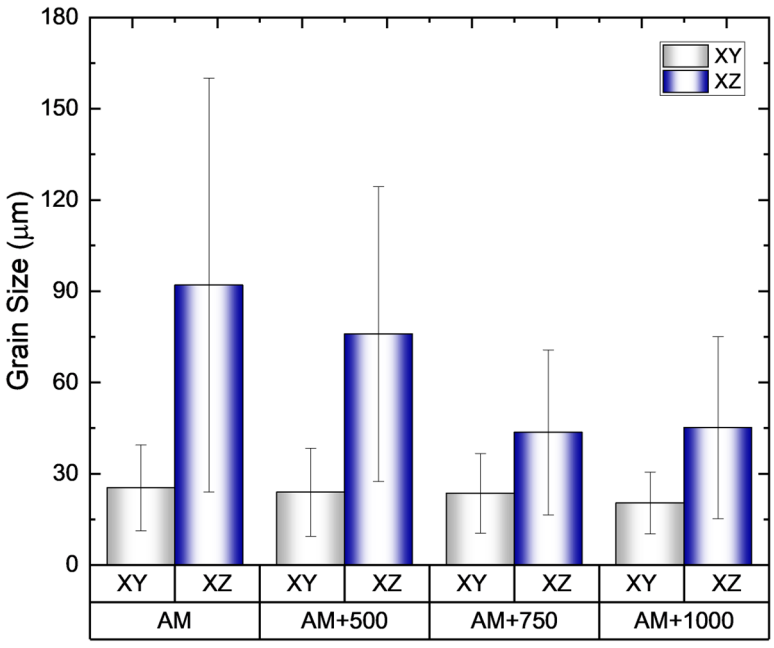

Figure 2. Grain size comparison of the AF and AF + aged samples at different heat treatment temperatures and for XY and XZ planes.

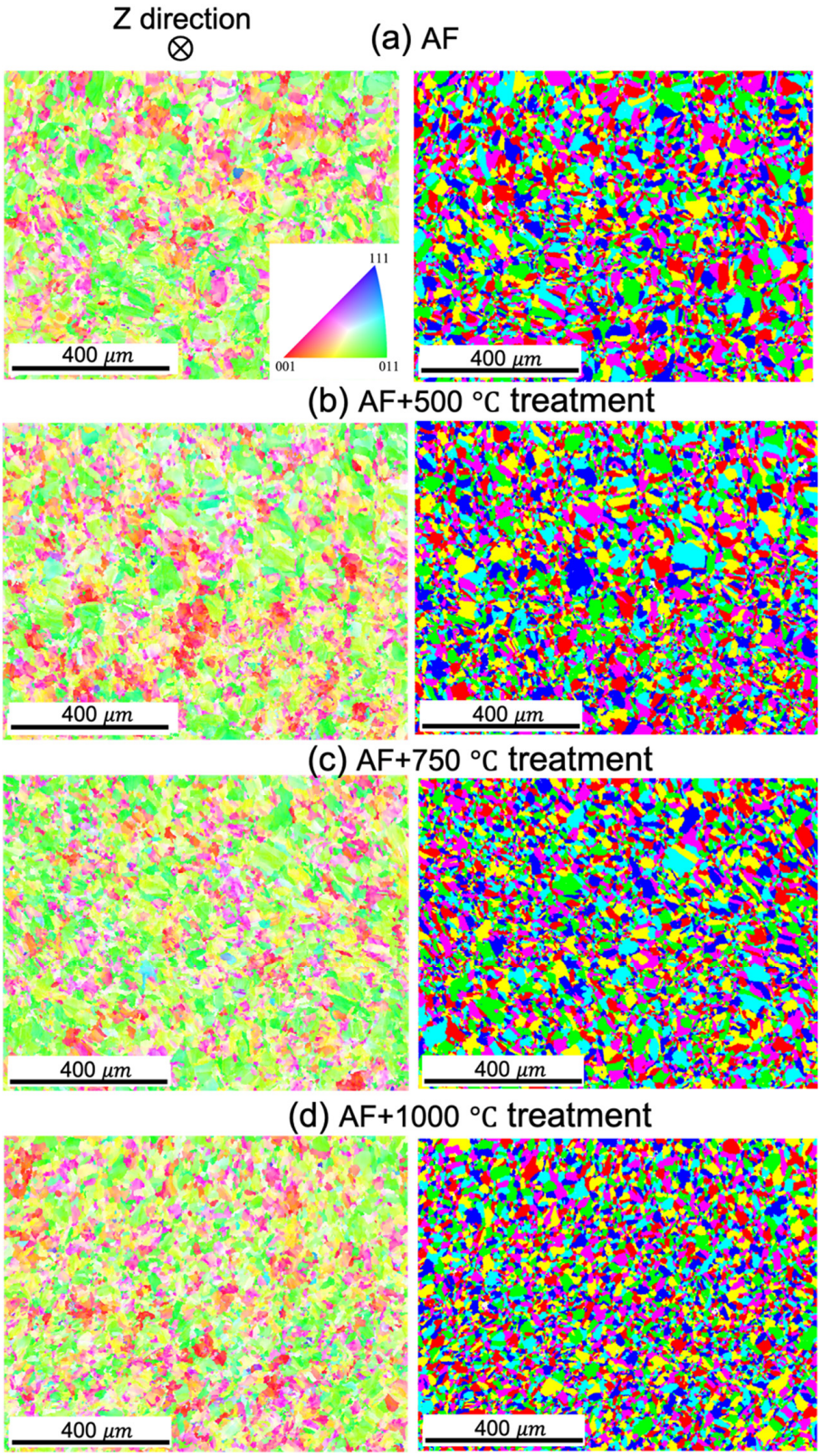

Figure 3. XZ plane EBSD-IPF images (**left**) and grain structures (**right**) of the AF and AF + aged samples at different heat treatment temperatures, as shown in the subfigures (**a**–**d**).

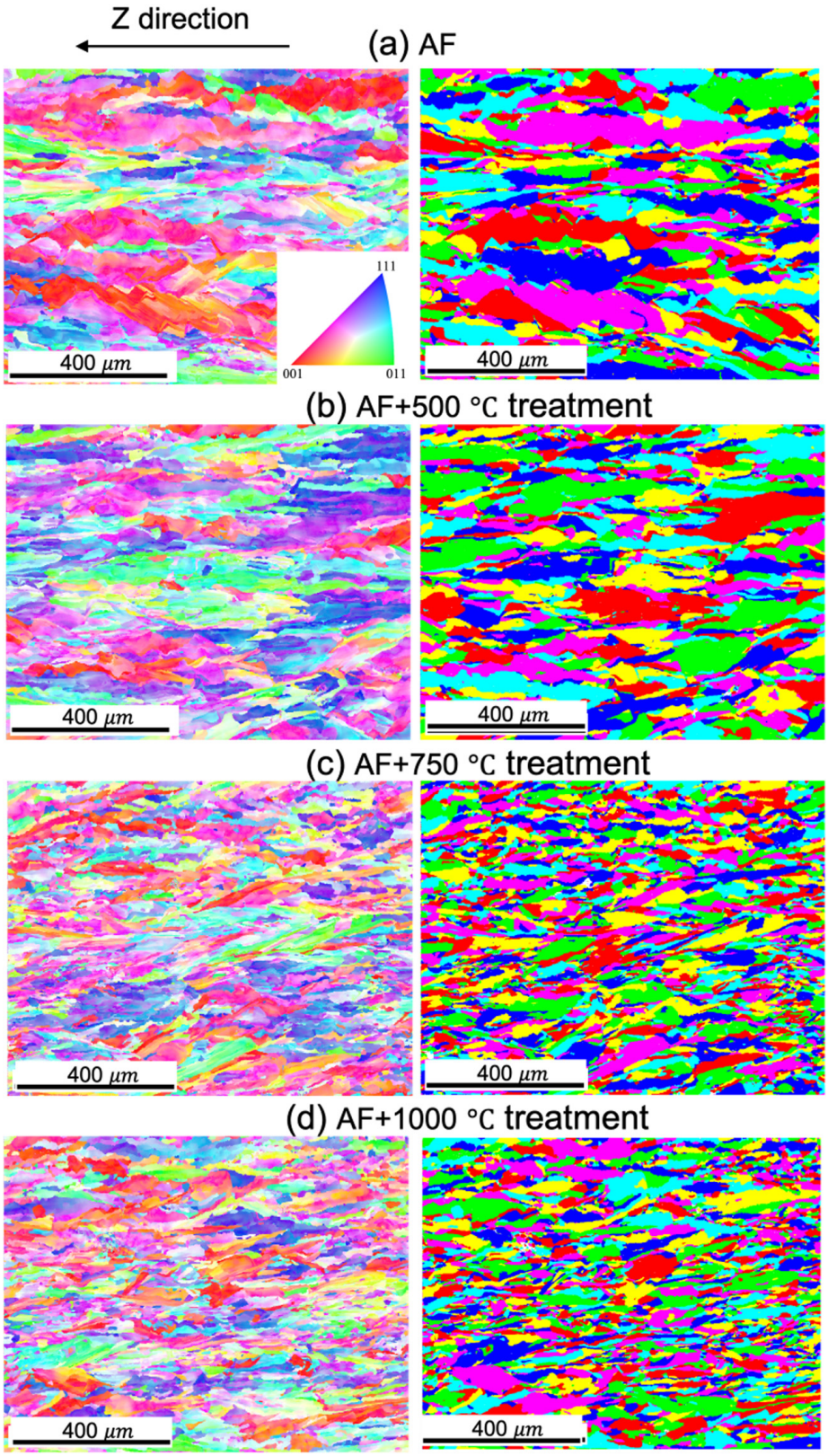

Figure 4. EBSD-IPF images (**left**) and grain structures (**right**) of the AF and AF + aged samples on the XZ plane at different heat treatment temperatures, as shown in the subfigures (**a**–**d**).

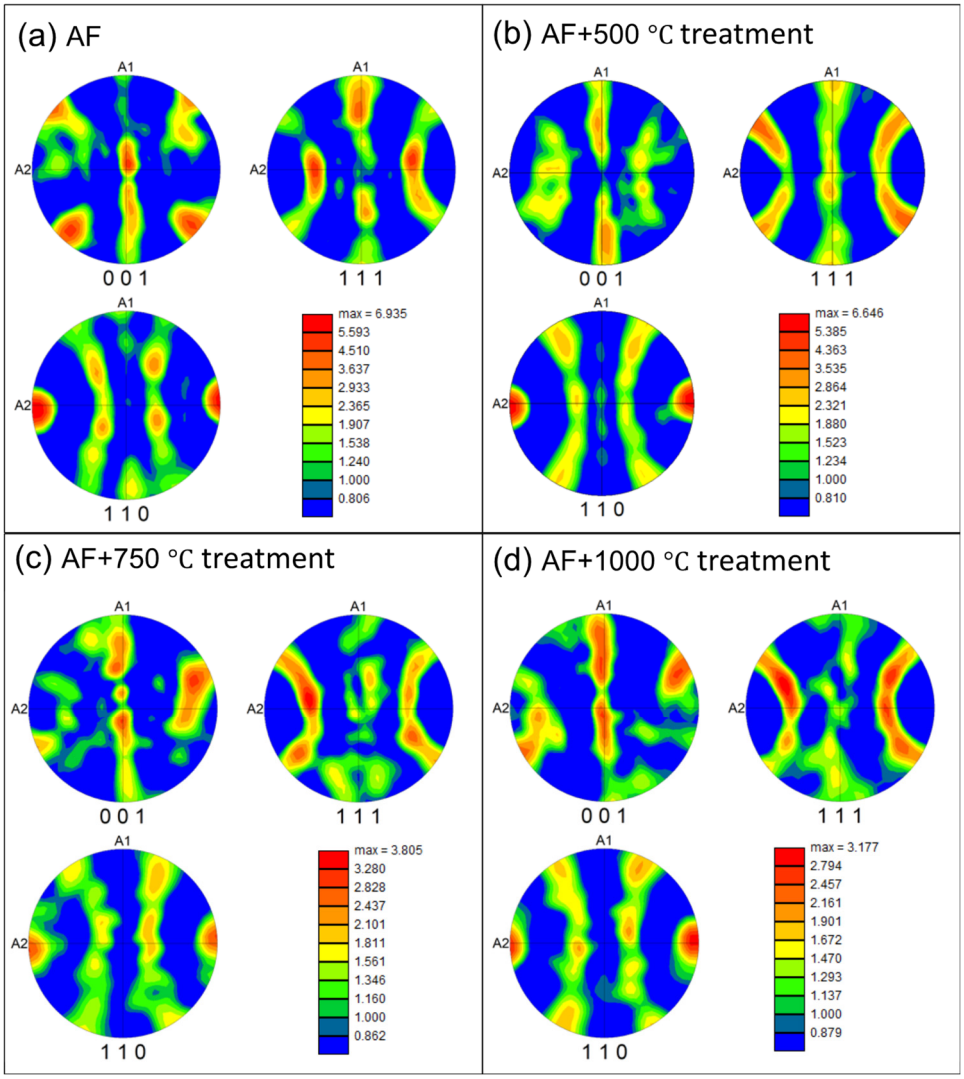

Figure 5. Pole-figure images of the AF and AF + heat-treated samples on the XZ plane at different heat treatment temperatures, as shown in the subfigures (**a**–**d**); A1 and A2 corresponds to the X and Z directions, respectively.

The TEM images shown in Figure 6 demonstrate the existence of high dislocation networks, which were significantly higher than traditionally wrought samples. This is attributed to the substantial residual stresses induced by the rapid cooling phase of the LPBF process [31]. As the temperature increases, the density of dislocation networks reduces. Notably, the dislocation networks almost disappear for the AF + aged 1000 °C sample. The dislocation cell diameters were 325 ± 23 nm, 370 ± 44 nm, and 415 ± 54 nm for AF, AF + 500, and AF + 750, respectively. The dislocation density was estimated using the diameter of the dislocation cells obtained from TEM images, a method described in [32], which states $\lambda = B \cdot \rho^{-0.5}$, where ρ is dislocation density, λ is cell size, and B is material dependent constant. For 316L, B = 2. While this approach may introduce an error range within an order of magnitude, it provides a reliable general estimation. The calculated dislocation densities for the samples were 4×10^{13} m^{-2}, 3×10^{13} m^{-2}, and 2×10^{13} m^{-2} for AF, AF + 500, and AF + 750, respectively. These values align well with the range reported in earlier studies [32,33].

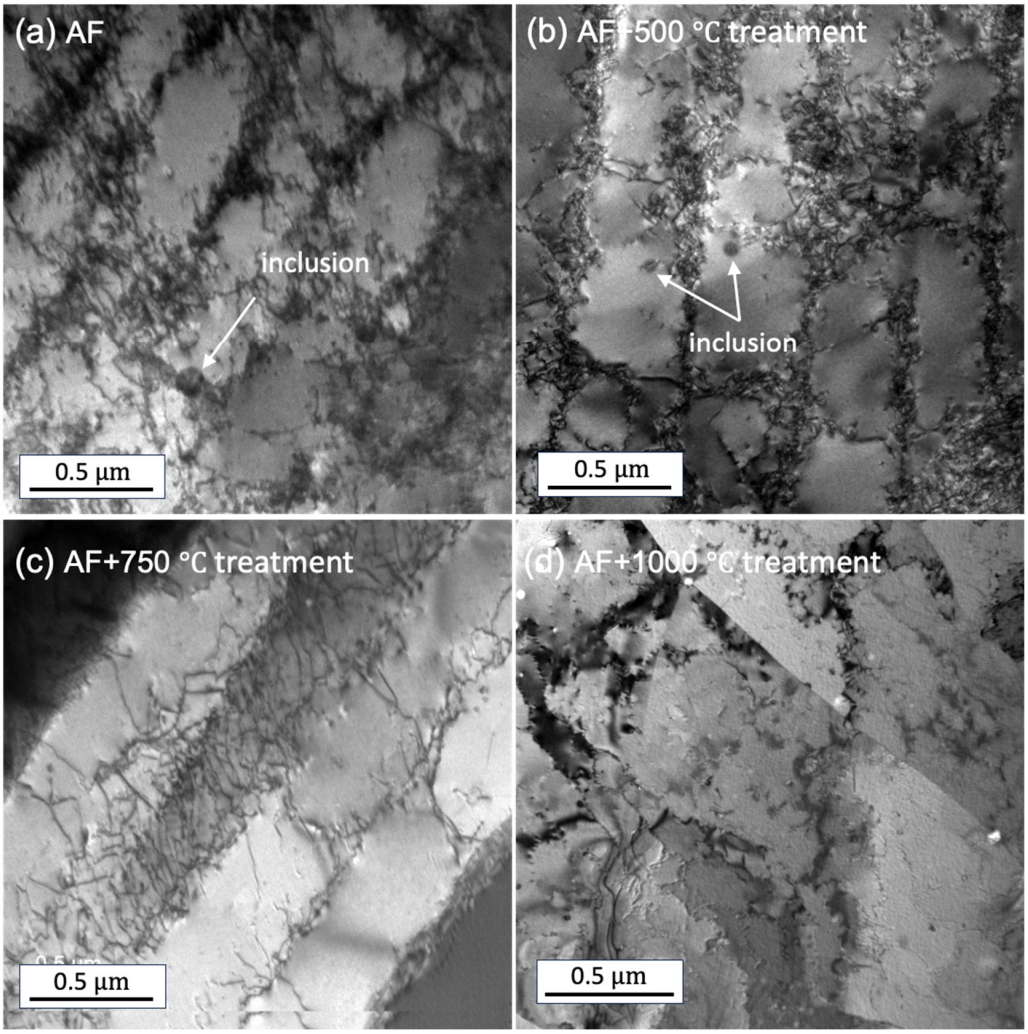

Figure 6. TEM images of the AF and AF + aged samples at different heat treatment temperatures, as shown in the subfigures (**a**–**d**).

The observed trend indicates a gradual decrease in dislocation density with increasing heat treatment temperature. This behavior is likely attributed to the recovery and partial annihilation of dislocations at elevated temperatures, which facilitate dislocation rearrangement and a reduction in internal strain energy. The nanometer-sized inclusions observed in the AF samples were almost negligible for the AF + aged 1000 °C sample. This result contrasts with [34], where inclusions were reported to be coarsened with an increase in temperature.

It is worth noting that, under both the AF and AF + aged conditions, no significant micro-segregation has been observed around the fusion boundary or dislocation sub-grain boundaries.

3.1.2. Electrochemical Analysis

The cyclic polarizations of the as-printed and heat-treated steels in 3.5% NaCl solution are shown in Figure 7. The repassivation potential (E_{rp}) signifies the capability to halt the pit's growth rate, while the pitting potential (E_p) is the minimum potential at which the material inclines toward pitting corrosion [35]. Beyond this potential, additional voids within the pit will initiate and enlarge. The local corrosion rate is indicated by the amount of hysteresis, or, to put it another way, by the difference between E_p and E_{rp}. Considering that the area of the hysteresis loop of the sample annealed at 750 °C is the lowest, it can

be said that the possibility of pitting corrosion in this sample is less than the others. As can be seen from Figure 7c, although there is no noticeable variation in corrosion potential for all samples (−112 mV), the corrosion rate of the LPBF-XZ plane (22.68 × 10^{-9} A) is around two times the XY (12.26 × 10^{-9} A). The rationale behind this observation is the diminutive gain size characteristic of the XY plane microstructure. In addition to Mo, the high diffusion rate of Cr along the grain boundary could promote the growth and repair of a high-resistance oxide layer rich in chromium (III) oxide.

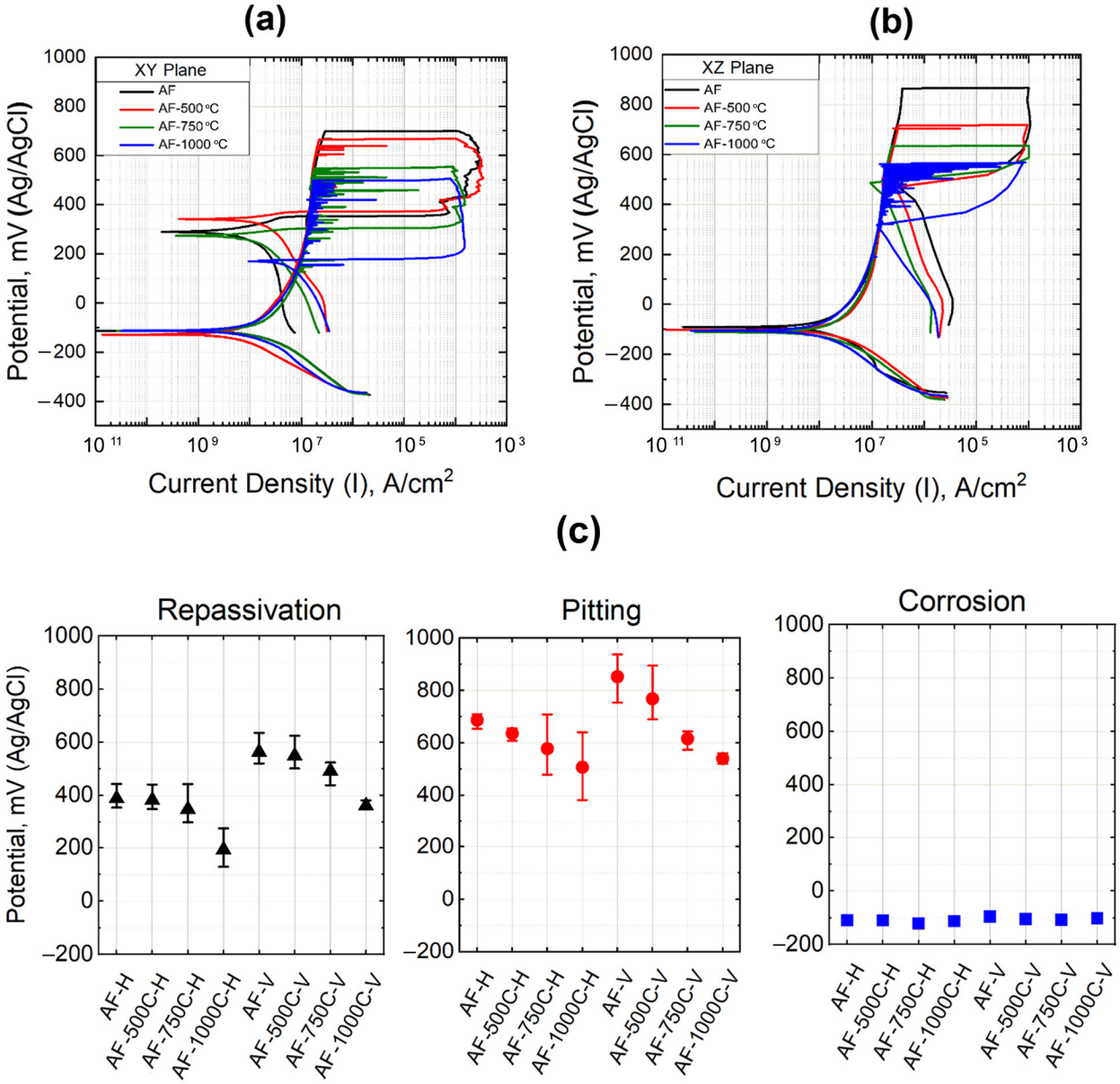

Figure 7. Cyclic polarization for planes (**a**) XY and (**b**) XZ are shown, and (**c**) repassivation potential, pitting potential, and corrosion potential extracted from the cyclic polarization curves for AF and AF + aged samples of H (XY horizontal plane) and Y (XZ vertical plane).

The fluctuation on the polarization curves in Figure 7a,b indicates the occurrence of metastable pitting, which is more prominent in the XZ plane (vertical plane). Frankel et al. [35] claim that the protective passive coating breaks down during the rate-controlling pitting stage. An initiated pit may propagate during pitting for a brief period of time before "dying", or it may propagate virtually endlessly (stable pitting) [36].

The pitting potentials dropped with heat treatment, and with increasing the heat treatment temperature, these values even dropped further. This reduction is more prominent for LPBF-XZ. The as-printed sample and the sample annealed at 500 °C on the XZ plane demonstrated a higher pitting potential than the horizontal one (XY plane). It was found that the repassivation potential showed a similar trend to the pitting potential. These values for the LPBF-XY and XZ samples are 397.1 and 564.3 mV, respectively. It is evident that the average repassivation potential in the horizontal XY plane is lower than in the vertical XZ plane and this value in both planes decreases proportionately with heat treatment. One noteworthy observation is that, after repassivation, the corrosion rate in the XY plane is significantly lower than that of the XZ plane (Figure 7b). That is to say, the repassive ability was always stronger on the XY plane.

Figure 8 shows the EIS results of the horizontal and vertical plane specimens in 3.5% NaCl solution. Figure 8a,b correspond to the bode plots of the XY and XZ planes, respectively. As can be seen, the impedance for the XY plane at its highest frequency is approximately 2×10^6 Ω·cm^2, meaning that it is approximately 1.25 times greater than that of the XZ plane (1.6×10^6 Ω·cm^2). The stainless steels that have undergone heat treatments seem to have a depressed impedance, and the higher the treatment temperature, the lower the impedance.

The Nyquist and Bode plots of the XY sample, along with the heat-treated samples at OCP, +100 mV, +200 mV, and +300 mV of anodic overpotential, shown in Figure 8b, indicates that the application of anodic polarization causes the capacitive loop to enlarge (Nyquist plot). Generally speaking, a large semicircle in the Nyquist plot indicates that there is more difficulty in transferring electrons from the substrate to the solution, and the loop's high capacitance suggests a relationship between the formation of the passive oxide layer and the charging of the electric double layer [37]. Due to this phenomenon, impedance increases significantly at 10^{-3} frequency, resulting in the following sequence of impedance values: OCP < OCP + 100 mV < OCP + 200 mV < OCP + 300 mV. Similarly, the XZ plane exhibited a comparable pattern.

In order to supplement the qualitative analysis, impedance parameters can be obtained through an equivalent circuit analysis, as illustrated in Figure 8c. In such a circuit, R_s stands for the electrolyte resistance. The double-layer capacitance and charge transfer are denoted by CPE and R_{ct}, respectively. An additional factor to take into account is that the mass transfer impedance, also known as the Warburg impedance, manifests as a line at low frequencies on the Nyquist diagram and can play a substantial role in the total internal resistance [37,38]. As depicted in Figure 8d, as the potential rises above the OCP, there is a notable increase in charge transfer resistance across all samples. This indicates a deceleration in the kinetics of the electrochemical process. As can be seen, the resistance of the double layer in the XY plane is higher than XZ, which can be a confirmation of the low corrosion rate in this plane. It is evident that when the treatment temperature rises, the double layer's resistance first achieves its maximum at 750 °C before beginning to decline. When the potential rises in relation to OCP, this increase becomes more apparent such that at 300 mV above OCP, the XY and XZ samples annealed at 750 °C have a resistance of 10.28×10^6 Ω and 7.32×10^6 Ω, respectively. Following 750 °C, samples annealed at 500 °C and 1000 °C have the highest passive layer resistance. It should be noted that raising the overpotential above 300 mV in relation to OCP resulted in a rather discernible change in the double layer's resistance.

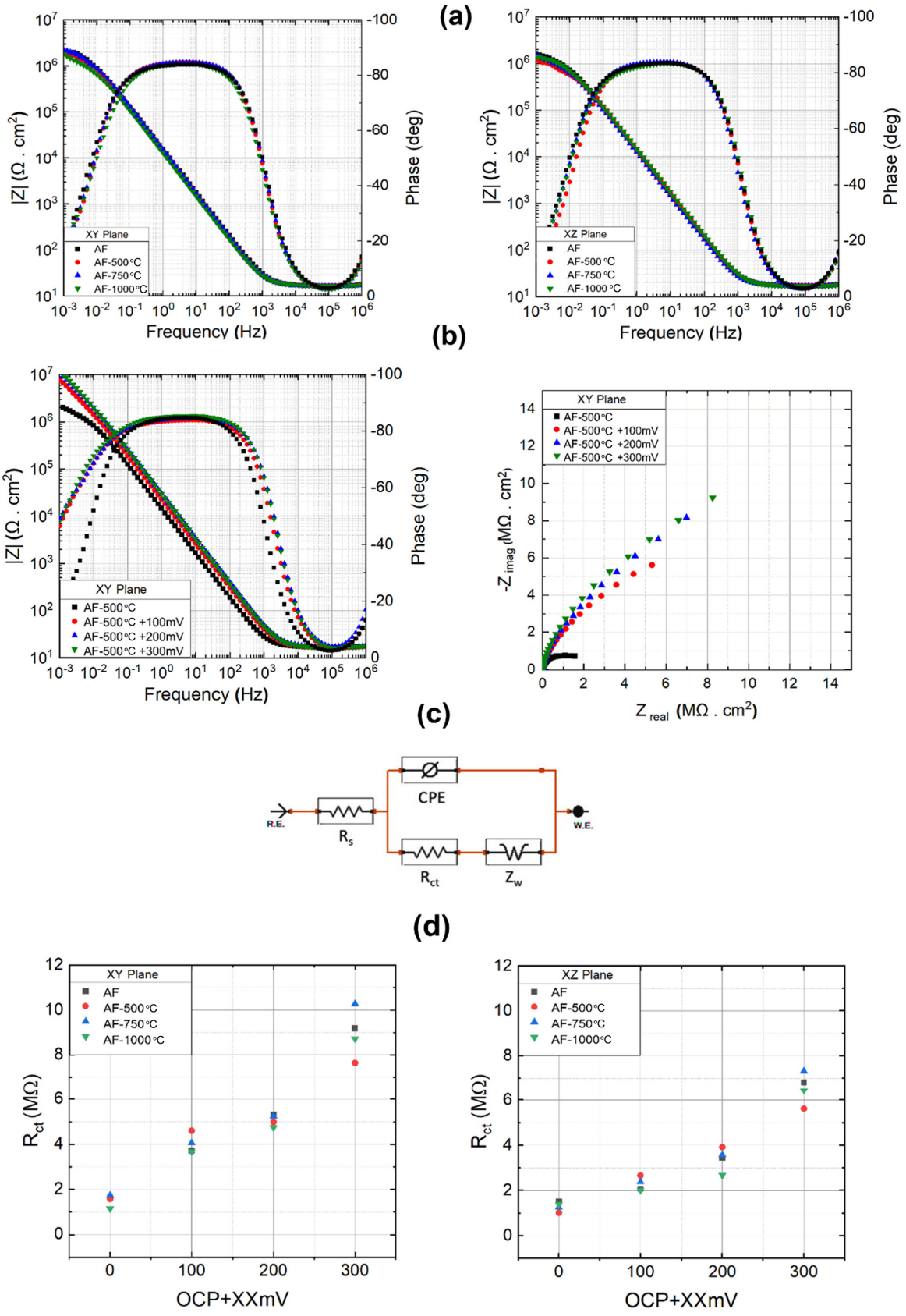

Figure 8. EIS results of the AF and AF + aged samples: (**a**) Bode plots of the XY and XZ planes, (**b**) Bode and Nyquist plots of the XY plane, (**c**) equivalent circuit for fitting the EIS results, and (**d**) extracted charge transfer resistance (R_{ct}) from the fitting to equivalent circuit.

3.2. Discussion

The key microstructural features observed in the AF samples during heat treatment are the refined grain structures and reduced dislocation densities with increasing heat treatment temperature (refer to Figures 2–4 and 6). The visibility of the melt pool boundaries up to 500 °C and their subsequent fading at higher temperatures (750 °C and 1000 °C) is accompanied by drastically reduced dislocation densities (Figure 6), indicating a higher dislocation mobility above 500 °C, facilitating a transition in the microstructural characteristics. The distinct grain is characterized by a misorientation angle of 15° relative to the adjacent grains. The reduction in grain size with increasing heat treatment temperature contradicts the grain growth around the same temperature range, as reported in [30,39]. At all the different heat treatment temperatures, the grain shape remains mostly columnar and elongated along the build direction, regardless of the reduced grain size and increased number of grains. The fine grains with varying crystallographic orientations develop from the original, larger columnar grains. Despite their smaller size, these newly formed grains retain a columnar shape, which is a distinctive feature compared to the more typical equiaxed grain structure that usually forms during static recrystallization. Additionally, sub-grain dislocation networks also play crucial roles in the development of high-angle grain boundaries. These networks of dislocations, which are localized regions of crystallographic misorientation within the grains, could contribute to the establishment of high-angle boundaries between neighboring grains, as they facilitate the movement of atoms and dislocations across the grain boundaries.

The as-printed texture of the material also results in anisotropic corrosion behavior. In the as-printed state, the XY (horizontal) plane exhibits significantly lower pitting potentials compared to the XZ (vertical) plane. The superior pitting resistance of the vertical plane gradually diminishes as the heat treatment temperature increases. At treatment temperatures of 750 °C and 1000 °C, the pitting potentials of the XY and XZ planes become nearly identical. Several factors could contribute to this phenomenon. Due to the columnar-shaped grains, the XY plane possesses a higher number of grains per unit area compared to the XZ plane, resulting in a larger area of grain boundaries. Grain boundaries are defective sites with an increased susceptibility to pitting [40,41]. Thus, the higher pitting potential of the XZ plane could be attributed to the smaller area of grain boundaries. In addition, the horizontal planes of the sample are primarily oriented along the ⟨011⟩ crystal directions, while the vertical planes exhibit a more random crystallographic orientation. This crystallographic anisotropy could significantly influence the pitting resistance. However, the specific relationship between crystallographic orientation and pitting resistance in LPBF cubic materials requires further investigation.

With an increasing annealing temperature, the larger number of grain sizes and, consequently, high-angle grain boundaries are responsible for the reduced pitting potentials on both the horizontal and vertical planes. In addition to the grain size effect, the reduced density of dislocation sub-grains also contributes to the decreased pitting and repassivation resistance with increasing heat treatment temperatures. Previous studies have highlighted the beneficial effect of sub-grain dislocation cellular/columnar structures [6,42] in the anti-corrosion resistance of 316L. Due to the general ⟨100⟩ orientation of the sub-grain boundaries and the strong texture developed in the as-built condition [43,44], the dislocation sub-grains intersect with the XY and XZ planes predominately in the form of cellular structures. Thus, the diminution of sub-grain dislocations, together with the increase in high-angle grain boundaries, contributes to the reduced pitting resistance.

In terms of passivity and repassivity, the XY plane shows a more significant reduction in corrosion rate during the reverse scan, indicating a more effective repassivation process compared to the XZ plane, despite the XY plane having a lower repassivation potential. In

contrast, repassivation on the XZ plane is incomplete, as the reverse scanning curves never return to the anodic region. The electrochemical impedance spectroscopy (EIS) results further reinforce these observations, showing that the XY plane has a higher charge transfer resistance (R_{ct}) at all elevated potentials, indicating a more stable passive film compared to the XZ plane. From the equivalent circuit analysis (Figure 7c), the R_{ct} and CPE directly correlate to the stability and resistance of the passive oxide layer. For the XY plane, the R_{ct} reached a peak value of 10.28×10^6 $\Omega \cdot cm^2$ at 750 °C, significantly higher than the XZ plane's maximum of 7.32×10^6 $\Omega \cdot cm^2$ under the same conditions. This indicates that the grain size and orientation of the XY plane contribute to a more stable and uniform passive film, reducing electron transfer kinetics and enhancing corrosion resistance.

The XY plane exhibits more uniform and refined grains, as well as a higher area of grain boundaries, than the XZ plane. Both grain boundaries and dislocation networks act as fast diffusion pathways, likely promoting the formation of a more stable and protective passive film, as well as aiding its repair after pitting. Consequently, the XY plane exhibits higher charge transfer resistance, indicating a more robust passive film compared to the XZ plane. This results in more effective repassivation on the XY plane, further enhancing its corrosion resistance relative to the XZ plane.

Thus, the seemingly controversial anisotropic pitting and repassivation behaviors may be related to the complex roles played by both the grain boundaries and dislocation networks, as discussed above.

Figure 9 shows the pitting morphologies of the AF and AF + aged 316L stainless steel post-cyclic polarization tests. Notably, the pits exhibit a predominantly spherical shape across all examined specimens on the XY plane. The pits on the XZ plane show a more irregular shape. The inhomogeneity may be related to the grain orientation-dependent corrosion resistance. With thermal treatment at an increasingly higher temperature, the pits on the XZ planes become narrower in the opening and deeper in penetration depth, confirming the weakened corrosion resistance. Additionally, it was not observed that pitting preferentially grows along the grain boundary or the melt pool boundaries. This could be related to negligible segregation near the grain boundaries and melt pools.

Previous studies [21,34,45] have highlighted the presence of nanoscale inclusions within 316L produced by L-PBF. Consistent with those reports, no microscale inclusions or precipitates were found in the as-printed or heat-treated states. These observations suggest that micro-inclusions were not the principal factors initiating pitting. Similar to previous reports [34,46,47], nanoparticles have been found in the AF condition. Saeidi et al. [47] observed a reduction in silicon and chromium concentrations surrounding circular nano-inclusions, suggesting that the creation of these inclusions involved the absorption of these elements from adjacent regions. However, determining whether pitting corrosion initiated at the inclusion sites was challenging through post-examination observations [48]. It has been reported that the presence of nanoscale inclusions is less likely to contribute detrimentally to corrosion performance [16,47,49].

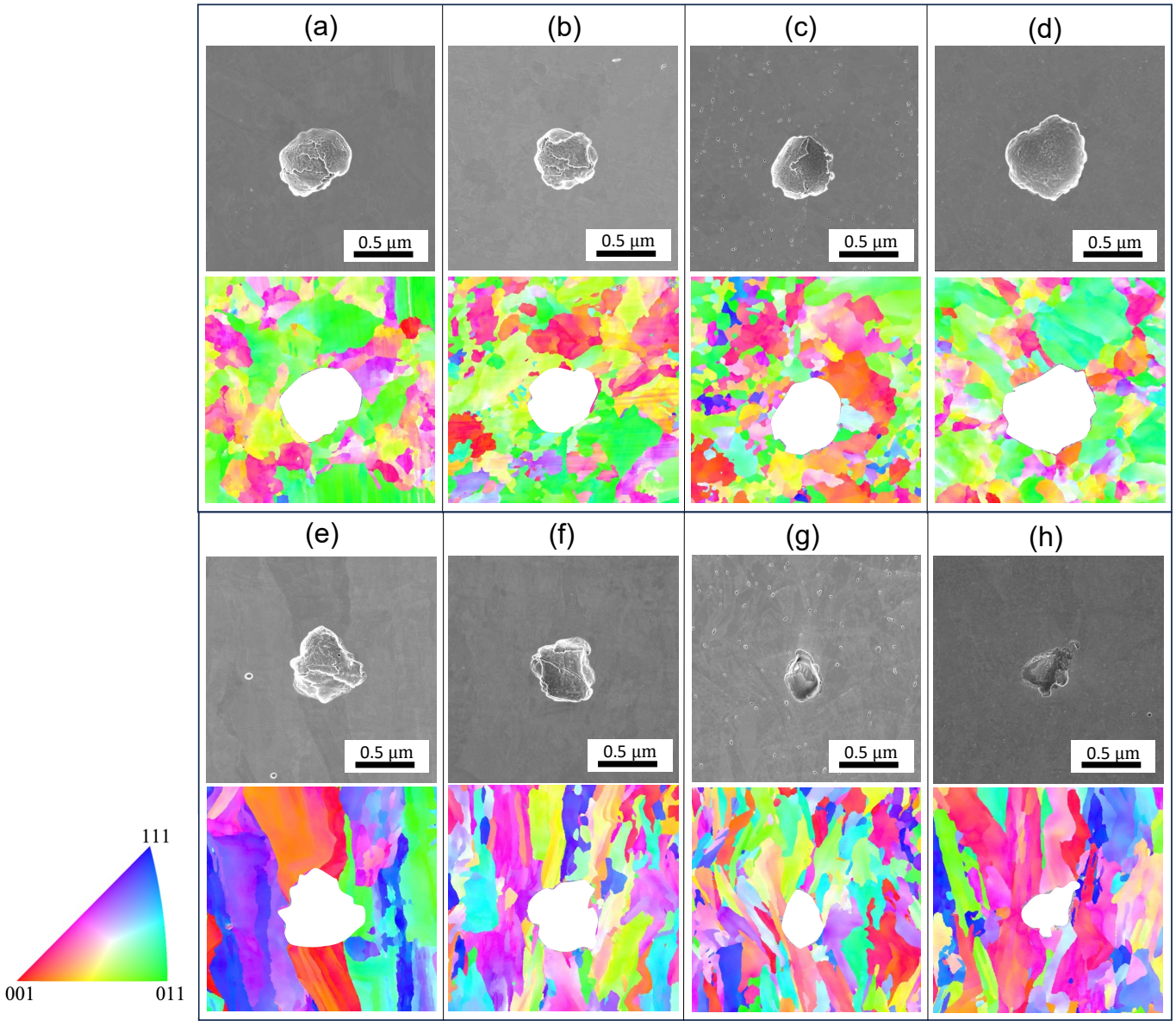

Figure 9. SEM, EBSD, and IPF correlation figures of the AF and AF + aged pit samples at different heat treatment temperatures, as shown in the subfigures: (**a**–**d**) correspond to the AF, AF + 500 °C, AF + 750 °C, and AF + 1000 °C on the XY plane; (**e**–**h**) correspond to the AF, AF + 500 °C, AF + 750 °C, and AF + 1000 °C on the XZ plane.

4. Conclusions

In this work, the effects of post-fabrication heat treatment on 316L, fabricated by L-PBF, on the aspects of microstructural features and corrosion performance, particularly considering treatments at 500 °C, 750 °C, and 1000 °C, were evaluated. The main findings are summarized as follows:

1. The microstructures are significantly altered during the heat treatment. The changes include diminished melt pool boundaries and dislocation of cellular structures, along with a reduced grain size, with increasing treatment temperatures. The grains remained elongated and columnar-shaped during the process.
2. A deterioration in corrosion resistance with an increased annealing temperature was evidenced by reduced pitting and repassivation potentials.
3. Anisotropic corrosion resistance was also observed. The vertical plane (parallel to the build direction) exhibited a higher pitting and repassivation potential, yet a higher

current density was observed post-repassivation. The degree of anisotropy gradually diminished with increasing treatment temperature.

4. The increased grain boundaries and reduced dislocation cell densities are attributed to the different corrosion performances after heat treatment.

The main findings of this research contribute to a deeper understanding of the post-fabrication processing–structure–property relationships in 316L stainless steel fabricated via L-PBF, pointing towards the importance of optimizing manufacturing and heat treatment parameters to enhance material performance in corrosive environments.

5. Practical Implementation

The findings provide critical guidelines for the additive manufacturing (AM) industry, particularly for sectors that require high-performance materials in corrosive environments, such as marine, chemical processing, and energy applications.

1. Industries producing components for applications demanding corrosion resistance, such as marine industries, should prioritize low-temperature heat treatments (500 °C). This temperature regime achieves microstructural homogenization and stress relief without introducing adverse grain growth and comprises pitting and repassivation behaviors.
2. Anisotropic corrosion behavior suggests that designers should strategically orient critical components during fabrication. Vertical orientations, with their demonstrated susceptibility to higher corrosion currents, may require additional surface treatments or coatings to ensure long-term durability in aggressive environments.
3. The main findings of this research contribute to a deeper understanding of the post-fabrication processing–structure–property relationships in 316L stainless steel fabricated via L-PBF, pointing towards the importance of optimizing manufacturing and heat treatment parameters to enhance material performance in corrosive environments.

6. Future Work

We aim to further understand the mechanisms of grain size reduction during heat treatment. Furthermore, the microstructural variations and the effects of heat treatment on the corrosion fatigue properties of 316L will also be a focus of our study. In addition, the precipitation and inclusion behavior during prolonged heat treatment and their effect on corrosion-related performance will be examined. Along with electrochemical tests, immersion tests in a ferric chloride solution at different controlled temperatures will be conducted. The distribution of pits on the sample surface after testing will be statistically analyzed, and other corrosion products will be carefully examined after different immersion durations to elucidate the role played by various microstructural features, such as grain boundaries and inclusions.

Author Contributions: Validation, formal analysis, investigation, data curation, writing—original draft, writing—review and editing, and visualization, K.S.; formal analysis, investigation, data curation, writing—original draft, and writing—review and editing, M.N.; conceptualization, investigation, resources, writing—review and editing, and supervision, J.S.; conceptualization, methodology, resources, writing—review and editing, supervision, project administration, and funding acquisition, Y.F. All authors have read and agreed to the published version of the manuscript.

Funding: The authors gratefully acknowledge the National Science Foundation (Award No. 2139383 and Award No. 2245107) and the Office of Naval Research (Award No. N00014-21-1-2800) for providing financial support.

Data Availability Statement: The data presented in this study are available on request from the corresponding author. The data are not publicly available due to privacy or ethical restrictions.

Acknowledgments: This work utilized the Nanoscale Characterization and Fabrication Laboratory, a part of the National Nanotechnology Coordinated Infrastructure (NNCI), funded by NSF (ECCS 1542100 and ECCS 2025151).

Conflicts of Interest: The authors declare no conflict of interest.

References

1. Sumita, M.; Hanawa, T.; Teoh, S. Development of nitrogen-containing nickel-free austenitic stainless steels for metallic biomaterials—Review. *Mater. Sci. Eng. C* **2004**, *24*, 753–760. [CrossRef]
2. Imbaby, M.; Jiang, K.; Chang, I. Net shape fabrication of stainless-steel micro machine components from metallic powder. *J. Micromech. Microeng.* **2008**, *18*, 115018. [CrossRef]
3. Choi, J.-P.; Shin, G.-H.; Brochu, M.; Kim, Y.-J.; Yang, S.-S.; Kim, K.-T.; Yang, D.-Y.; Lee, C.-W.; Yu, J.-H. Densification behavior of 316L stainless steel parts fabricated by selective laser melting by variation in laser energy density. *Mater. Trans.* **2016**, *57*, 1952–1959. [CrossRef]
4. Salman, O.O.; Funk, A.; Waske, A.; Eckert, J.; Scudino, S. Additive manufacturing of a 316L steel matrix composite reinforced with CeO_2 particles: Process optimization by adjusting the laser scanning speed. *Technologies* **2018**, *6*, 25. [CrossRef]
5. Kurgan, N.; Varol, R. Mechanical properties of P/M 316L stainless steel materials. *Powder Technol.* **2010**, *201*, 242–247. [CrossRef]
6. Gnanasekaran, B.; Song, J.; Vasudevan, V.; Fu, Y. Corrosion fatigue characteristics of 316L stainless steel fabricated by laser powder bed fusion. *Metals* **2021**, *11*, 1046. [CrossRef]
7. Pragana, J.P.; Pombinha, P.; Duarte, V.R.; A Rodrigues, T.; Oliveira, J.P.; Bragança, I.M.; Santos, T.G.; Miranda, R.M.; Coutinho, L.; Silva, C.M. Influence of processing parameters on the density of 316L stainless steel parts manufactured through laser powder bed fusion. *Proc. Inst. Mech. Eng. Part B J. Eng. Manuf.* **2020**, *234*, 1246–1257. [CrossRef]
8. Ziri, S.; Hor, A.; Mabru, C. Combined effect of powder properties and process parameters on the density of 316L stainless steel obtained by laser powder bed fusion. *Int. J. Adv. Manuf. Technol.* **2022**, *120*, 6187–6204. [CrossRef]
9. Huang, G.; Wei, K.; Deng, J.; Liu, M.; Zeng, X. High-power laser powder bed fusion of 316L stainless steel: Defects, microstructure, and mechanical properties. *J. Manuf. Process.* **2022**, *83*, 235–245. [CrossRef]
10. Piazza, S.; Merrigan, B.; Dowling, D.P.; Celikin, M. The effects of geometry and laser power on the porosity and melt pool formation in additively manufactured 316L stainless steel. *Int. J. Adv. Manuf. Technol.* **2020**, *111*, 1457–1470. [CrossRef]
11. Sander, G.; Thomas, S.; Cruz, V.; Jurg, M.; Birbilis, N.; Gao, X.; Brameld, M.; Hutchinson, C.R. On the corrosion and metastable pitting characteristics of 316L stainless steel produced by selective laser melting. *J. Electrochem. Soc.* **2017**, *164*, C250. [CrossRef]
12. Sun, Y.; Moroz, A.; Alrbaey, K. Sliding wear characteristics and corrosion behaviour of selective laser melted 316L stainless steel. *J. Mater. Eng. Perform.* **2014**, *23*, 518–526. [CrossRef]
13. Schaller, R.F.; Taylor, J.M.; Rodelas, J.; Schindelholz, E.J. Corrosion properties of powder bed fusion additively manufactured 17-4 PH stainless steel. *Corrosion* **2017**, *73*, 796–807. [CrossRef]
14. Geenen, K.; Röttger, A.; Theisen, W. Corrosion behavior of 316L austenitic steel processed by selective laser melting, hot-isostatic pressing, and casting. *Mater. Corros.* **2017**, *68*, 764–775. [CrossRef]
15. Song, J.; Sangoi, K.; Nadimi, M.; Fu, Y. Remarkably enhanced corrosion performance of 316 L stainless steel via laser powder bed fusion thin-layer deposition. *Mater. Today Commun.* **2024**, *38*, 107690. [CrossRef]
16. Laleh, M.; Hughes, A.E.; Xu, W.; Cizek, P.; Tan, M.Y. Unanticipated drastic decline in pitting corrosion resistance of additively manufactured 316L stainless steel after high-temperature post-processing. *Corros. Sci.* **2020**, *165*, 108412. [CrossRef]
17. DebRoy, T.; Wei, H.L.; Zuback, J.S.; Mukherjee, T.; Elmer, J.W.; Milewski, J.O.; Beese, A.M.; Wilson-Heid, A.D.; De, A.; Zhang, W. Additive manufacturing of metallic components–process, structure and properties. *Prog. Mater. Sci.* **2018**, *92*, 112–224. [CrossRef]
18. Sprouster, D.J.; Cunningham, W.S.; Halada, G.P.; Yan, H.; Pattammattel, A.; Huang, X.; Olds, D.; Tilton, M.; Chu, Y.S.; Dooryhee, E.; et al. Dislocation microstructure and its influence on corrosion behavior in laser additively manufactured 316L stainless steel. *Addit. Manuf.* **2021**, *47*, 102263. [CrossRef]
19. Trelewicz, J.R.; Halada, G.P.; Donaldson, O.K.; Manogharan, G. Microstructure and corrosion resistance of laser additively manufactured 316L stainless steel. *JOM* **2016**, *68*, 850–859. [CrossRef]
20. Ziętala, M.; Durejko, T.; Polański, M.; Kunce, I.; Płociński, T.; Zieliński, W.; Łazińska, M.; Stępniowski, W.; Czujko, T.; Kurzydłowski, K.J.; et al. The microstructure, mechanical properties and corrosion resistance of 316L stainless steel fabricated using laser engineered net shaping. *Mater. Sci. Eng. A* **2016**, *677*, 1–10. [CrossRef]
21. Kong, D.; Ni, X.; Dong, C.; Zhang, L.; Man, C.; Yao, J.; Xiao, K.; Li, X. Heat treatment effect on the microstructure and corrosion behavior of 316L stainless steel fabricated by selective laser melting for proton exchange membrane fuel cells. *Electrochim. Acta* **2018**, *276*, 293–303. [CrossRef]

22. Wang, K.; Chao, Q.; Annasamy, M.; Hodgson, P.D.; Thomas, S.; Birbilis, N.; Fabijanic, D. On the pitting behaviour of laser powder bed fusion prepared 316L stainless steel upon post-processing heat treatments. *Corros. Sci.* **2022**, *197*, 110060. [CrossRef]
23. Bedmar, J.; García-Rodríguez, S.; Roldán, M.; Torres, B.; Rams, J. Effects of the heat treatment on the microstructure and corrosion behavior of 316 L stainless steel manufactured by Laser Powder Bed Fusion. *Corros. Sci.* **2022**, *209*, 110777. [CrossRef]
24. Ronneberg, T.; Davies, C.M.; Hooper, P.A. Revealing relationships between porosity, microstructure and mechanical properties of laser powder bed fusion 316L stainless steel through heat treatment. *Mater. Des.* **2020**, *189*, 108481. [CrossRef]
25. Dong, P.; Vecchiato, F.; Yang, Z.; Hooper, P.; Wenman, M. The effect of build direction and heat treatment on atmospheric stress corrosion cracking of laser powder bed fusion 316L austenitic stainless steel. *Addit. Manuf.* **2021**, *40*, 101902. [CrossRef]
26. Kluczyński, J.; Śnieżek, L.; Grzelak, K.; Oziębło, A.; Perkowski, K.; Torzewski, J.; Szachogłuchowicz, I.; Gocman, K.; Wachowski, M.; Kania, B. Comparison of different heat treatment processes of selective laser melted 316L steel based on analysis of mechanical properties. *Materials* **2020**, *13*, 3805. [CrossRef] [PubMed]
27. Sun, C.; Xiao, R.; Li, H.; Ruan, Y. Effects of phase selection and microsegregation on corrosion behaviors of Ti-Al-Mo alloys. *Corros. Sci.* **2022**, *200*, 110232. [CrossRef]
28. Li, M.; Chen, W.-Y.; Zhang, X. Effect of heat treatment on creep behavior of 316 L stainless steel manufactured by laser powder bed fusion. *J. Nucl. Mater.* **2022**, *559*, 153469. [CrossRef]
29. Jinhui, L.; Ruidi, L.; Wenxian, Z.; Liding, F.; Huashan, Y. Study on formation of surface and microstructure of stainless steel part produced by selective laser melting. *Mater. Sci. Technol.* **2010**, *26*, 1259–1264. [CrossRef]
30. Zhou, C.; Hu, S.; Shi, Q.; Tao, H.; Song, Y.; Zheng, J.; Xu, P.; Zhang, L. Improvement of corrosion resistance of SS316L manufactured by selective laser melting through subcritical annealing. *Corros. Sci.* **2019**, *164*, 108353. [CrossRef]
31. Liu, Y.; Yang, Y.; Wang, D. A study on the residual stress during selective laser melting (SLM) of metallic powder. *Int. J. Adv. Manuf. Technol.* **2016**, *87*, 647–656. [CrossRef]
32. Feaugas, X.; Haddou, H. Effects of grain size on dislocation organization and internal stresses developed under tensile loading in fcc metals. *Philos. Mag.* **2007**, *87*, 989–1018. [CrossRef]
33. Bertsch, K.; de Bellefon, G.M.; Kuehl, B.; Thoma, D. Origin of dislocation structures in an additively manufactured austenitic stainless steel 316L. *Acta Mater.* **2020**, *199*, 19–33. [CrossRef]
34. Chao, Q.; Cruz, V.; Thomas, S.; Birbilis, N.; Collins, P.; Taylor, A.; Hodgson, P.D.; Fabijanic, D. On the enhanced corrosion resistance of a selective laser melted austenitic stainless steel. *Scr. Mater.* **2017**, *141*, 94–98. [CrossRef]
35. Frankel, G.S. Pitting Corrosion of Metals: A Review of the Critical Factors. *J. Electrochem. Soc.* **1998**, *145*, 2186–2198. [CrossRef]
36. Khamaj, J.A. Cyclic polarization analysis of corrosion behavior of ceramic coating on 6061 Al/SiCp composite for marine applications. *Prot. Met. Phys. Chem. Surfaces* **2016**, *52*, 886–893. [CrossRef]
37. Jüttner, K. Electrochemical impedance spectroscopy (EIS) of corrosion processes on inhomogeneous surfaces. *Electrochim. Acta* **1990**, *35*, 1501–1508. [CrossRef]
38. Pang, J.; Briceno, A.; Chander, S. A Study of Pyrite/Solution Interface by Impedance Spectroscopy. *J. Electrochem. Soc.* **1990**, *137*, 3447–3455. [CrossRef]
39. Salman, O.; Gammer, C.; Chaubey, A.; Eckert, J.; Scudino, S. Effect of heat treatment on microstructure and mechanical properties of 316L steel synthesized by selective laser melting. *Mater. Sci. Eng. A* **2019**, *748*, 205–212. [CrossRef]
40. Terada, M.; Saiki, M.; Costa, I.; Padilha, A.F. Microstructure and intergranular corrosion of the austenitic stainless steel 1.4970. *J. Nucl. Mater.* **2006**, *358*, 40–46. [CrossRef]
41. Terada, M.; Escriba, D.M.; Costa, I.; Materna-Morris, E.; Padilha, A.F. Investigation on the intergranular corrosion resistance of the AISI 316L(N) stainless steel after long time creep testing at 600 °C. *Mater. Charact.* **2008**, *59*, 663–668. [CrossRef]
42. Zhou, C.; Wang, J.; Hu, S.; Tao, H.; Fang, B.; Li, L.; Zheng, J.; Zhang, L. Enhanced corrosion resistance of additively manufactured 316L stainless steel after heat treatment. *J. Electrochem. Soc.* **2020**, *167*, 141504. [CrossRef]
43. Montero-Sistiaga, M.L.; Godino-Martinez, M.; Boschmans, K.; Kruth, J.-P.; Van Humbeeck, J.; Vanmeensel, K. Microstructure evolution of 316L produced by HP-SLM (high power selective laser melting). *Addit. Manuf.* **2018**, *23*, 402–410. [CrossRef]
44. Jeon, J.M.; Park, J.M.; Yu, J.-H.; Kim, J.G.; Seong, Y.; Park, S.H.; Kim, H.S. Effects of microstructure and internal defects on mechanical anisotropy and asymmetry of selective laser-melted 316L austenitic stainless steel. *Mater. Sci. Eng. A* **2019**, *763*, 138152. [CrossRef]
45. Ni, X.; Kong, D.; Wu, W.; Zhang, L.; Dong, C.; He, B.; Lu, L.; Wu, K.; Zhu, D. Corrosion behavior of 316L stainless steel fabricated by selective laser melting under different scanning speeds. *J. Mater. Eng. Perform.* **2018**, *27*, 3667–3677. [CrossRef]
46. Gorsse, S.; Hutchinson, C.; Gouné, M.; Banerjee, R. Additive manufacturing of metals: A brief review of the characteristic microstructures and properties of steels, Ti-6Al-4V and high-entropy alloys. *Sci. Technol. Adv. Mater.* **2017**, *18*, 584–610. [CrossRef] [PubMed]
47. Saeidi, K.; Gao, X.; Zhong, Y.; Shen, Z. Hardened austenite steel with columnar sub-grain structure formed by laser melting. *Mater. Sci. Eng. A* **2015**, *625*, 221–229. [CrossRef]

48. Schaller, R.F.; Mishra, A.; Rodelas, J.M.; Taylor, J.M.; Schindelholz, E.J. The role of microstructure and surface finish on the corrosion of selective laser melted 304L. *J. Electrochem. Soc.* **2018**, *165*, C234. [CrossRef]
49. Lodhi, M.; Iams, A.; Sikora, E.; Palmer, T. Microstructural features contributing to macroscopic corrosion: The role of oxide inclusions on the corrosion properties of additively manufactured 316L stainless steel. *Corros. Sci.* **2022**, *203*, 110354. [CrossRef]